SUPPLEMENTARY INFORMATION

Stretching-induced conductance variations as fingerprints of contact configurations in single-molecule junctions

Yong-Hoon Kim,[1,*] Hu Sung Kim,[1] Juho Lee,[1] Makusu Tsutsui,[2,*] and Tomoji Kawai[2]

[1]*Graduate School of Energy, Environment, Water, and Sustainability, Korea Advanced Institute of Science and Technology, 291 Daehak-ro, Yuseong-gu, Daejeon 305-701, Korea.*
[2]*The Institute of Scientific and Industrial Research, Osaka University, 8-1 Mihogaoka, Ibaraki, Osaka 567-0047, Japan.*

y.h.kim@kaist.ac.kr
makusu32@sanken.osaka-u.ac.jp

I. Supplementary Computational Data

A. Details of computational modeling and simulation methods

A.1 Static junction stretching simulations

In the static junction pulling simulations, L was defined as the distance between the innermost fixed layers of the top and bottom electrodes (third layers from the electrode surface), and the initial L distance (ΔL = 0.0 Å) was L_0 = 23.7 Å for the CN1-1, CN2-2, CN3-3, CN3-2, and CN2-1 models (Figure 2b). This distance was chosen such that the molecular length approximately corresponds to that obtained from a junction model based on perfectly flat Au electrodes (without any apex atom) that has been maximally stretched until a protruded Au surface atom is generated [39], in which the molecular length measured by the S-S distance was 9.4 Å. The L_0 distances for other models that include additional Au apex or chain atoms were determined by stretching the junctions and selecting when they form almost linear conformations: L_0 = 25.7 Å for the CN11-1 model and L_0 = 27.8 Å for the CN21-12, CN11-11, CN21-11, and CN111-1 models. Starting from L_0, we stretched each junction model along the surface-normal direction by retracting the fixed top and bottom outer three Au layers at the step of ΔL = 0.6 Å and successively optimizing the junction geometry.

A.2 Junction stretching molecular dynamics simulations

Starting from the CN3-3 junction models used in the static stretching studies (L_0 = 23.7 Å as ΔL = 0.0 Å), we eliminated the two outermost fixed layers in both top and bottom electrodes to reduce the calculation cost. In the canonical (*NVT*) ensemble at 300 K under a Nosé-Hoover thermostat [44], the junction models were first evolved for 1 ps with the 1 fs time step for equilibration. We next retracted the fixed top and bottom Au layers by the amount of ΔL = 0.4 Å

along the surface normal direction, and further MD time propagations were performed for Δt = 1 ps, approximately amounting the pulling speed of $v_d \approx 40$ m/s. These pulling and time evolution steps were successively repeated for the total of 27 ps to reach total ΔL = 10.8 Å before the rupture of the Au-Au bond within the Au monoatomic chain. Two additional MD simulations with different ΔL and Δt combinations were performed to check the reliability of the observed CN3 to CN21 conversion process. Then, six additional MD simulations were performed with ΔL = 0.4 Å and decreasing Δt (increasing pulling speed v_d), from which we observed the Au-S bond rupture before the CN3 to CN21 conversion at $v_d \approx 330$ m/s. The trends from MD simulations are summarized in Table S1.

B. Robustness of computational results: Au(111) electrode models and generalized gradient approximation data

The simulations discussed in the manuscript was based the Au(100) electrode model and local density approximation (LDA). Adopting the Au(111) surface model rather than the Au(100) one or the Perdew-Burke-Ernzerhof (PBE) generalized gradient approximation (GGA) rather than LDA, we have obtained the essentially identical pulling-induced energetic (Figs. S1, S2) and transport behavior (Figs. S3, S4). In the static junction pulling simulations for the Au(111) case, L was defined as the distance between the innermost fixed layers of the top and bottom electrodes (third layers from the electrode surface). The initial L distance (ΔL = 0.0 Å) for the CN1-1, CN2-2, CN3-2, CN2-1 models was L_0 = 27.0 Å, which is slightly longer than that in the Au(100) electrode case due to the difference in the crystal plane. The L_0 distances for other models that include additional Au apex or chain atoms were determined by stretching the junctions and selecting when they form almost linear conformations: L_0 = 29.4 Å for the CN11-1 model and L_0 = 31.7 Å for the CN21-12 and CN111-1 models, which were again longer than those in the Au(111) cases. Starting from L_0, we stretched each junction model along the surface-normal direction by retracting the fixed top and bottom outer three Au layers and successively optimizing the junction geometry.

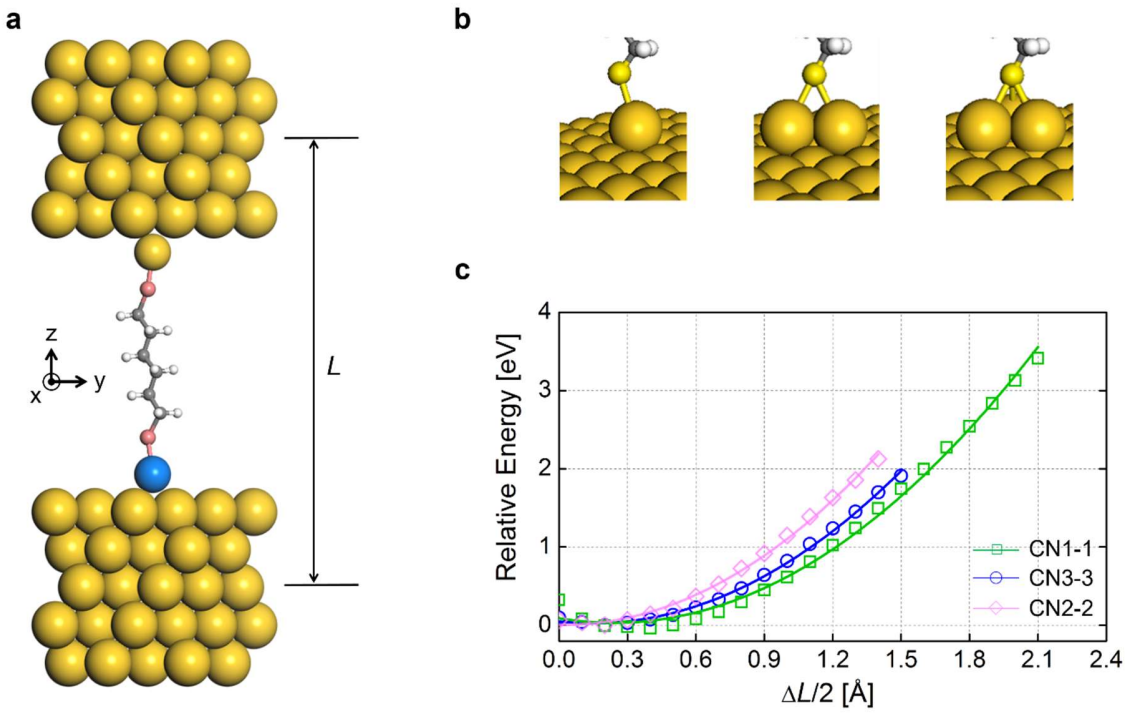

Figure S1 | Stretching-induced relative energy variations in the CN1-1, CN2-2, and CN3-3 models based on the Au(111) surface. (**a**) The CN1-1 Au-C6DT-Au junction model based on the Au(111) electrode. Here, *L* was defined as the distance between the top fixed layer of the bottom electrode and the bottom fixed layer of the top electrode. The lowercase *l* represents the Au-S bond length. (**b**) Considered contact atomic structure cases with different Au-S CNs that correspond to the bottom Au apex atom shown in blue in (a): CN1, CN2, and CN3 from left to right. (**c**) Stretching-induced relative energy variations of CN1-1, CN2-2, and CN3-3 models as the function of displacement (ΔL).

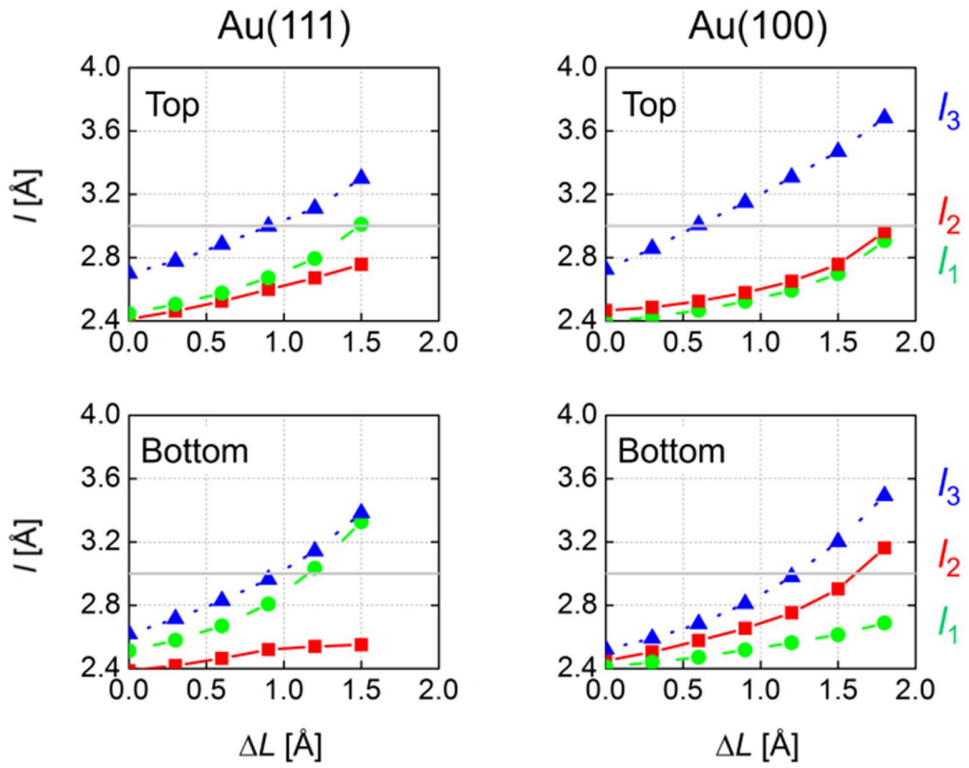

Figure S2 | Stretching-induced variations in the three Au-S bond lengths (*l*) for the CN3-3 case based on the Au(111) and Au(100) electrodes models. Under the stretching force, the CN3 bonding configurations assume CN2- or CN1-like contact geometries. Although the details of bond length development are different for the Au(100) and Au(111) cases, we can observe that even beyond the maximum Au-S bond distance of roughly 3.0 Å (shown as grey lines) the static junction pulling simulations employing zero-temperature geometry optimizations do not properly show bond ruptures or the Au apex atoms structural (or CN) changes .

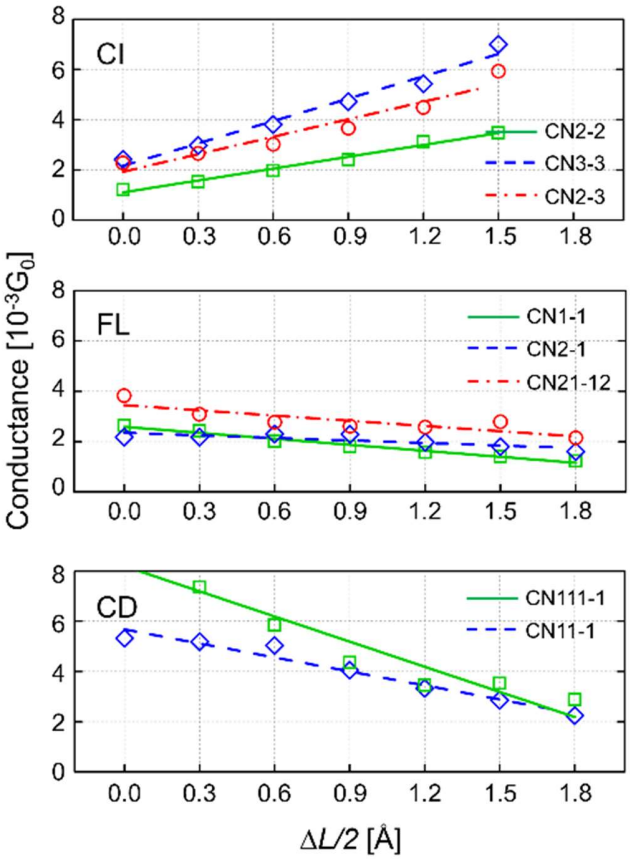

Figure S3 | Strain-dependent conductance variations grouped into three types, CI (top), FL (middle), and CD (bottom). For the Au(111) surface case, we observed the same conductance variation trend-contact atomic structure groupings as in the Au(100) counterpart: First, the CN2- or CN3-based junction models (CN2-2, CN3-3, and CN2-3) show the CI mode. Next, the CN1-based junctions (CN1-1, CN21-12, and CN2-1) can be associated with the FL mode. Finally, junction models involving Au monoatomic wire contacts (CN11-1 and CN111-1) exhibit the CD mode.

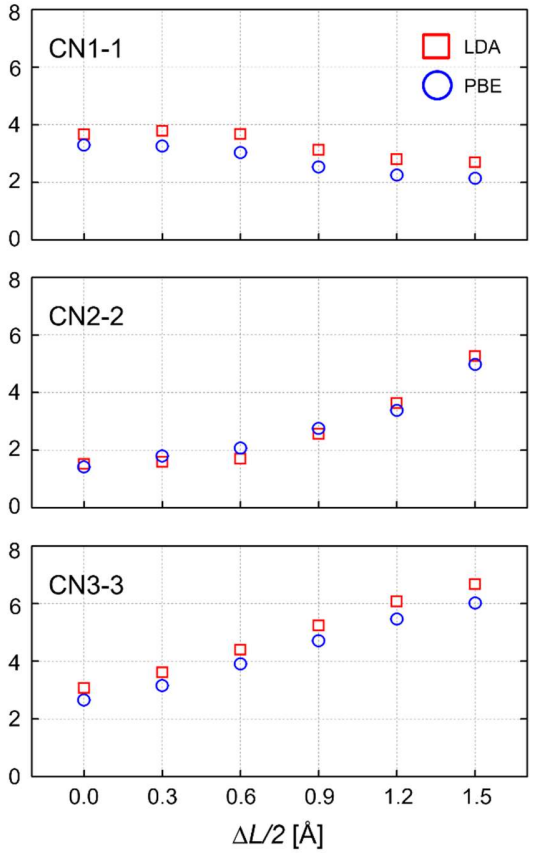

Figure S4 | Strain-dependent conductance variations within LDA and PBE GGA. The adaptation of PBE GGA exchange-correlation functional does not qualitatively or quantitatively modify the results obtained within LDA.

C. Computational results for the other models including mixed CN cases

In the case of symmetric CN2-2 junction model, we observe a behavior very similar to the CN3-3 case – namely, it shows a noticeable upshift of HOMO-related states with junction stretching. In the case of asymmetric CN11-1 junction model, comparing with the CN1-1 and CN11-11 data (Fig. 3), we observe that its PDOS more closely resembles the CN11 PDOS rather than the CN1 PDOS, explaining why CN11-1 exhibits the CD mode rather than the FL one. Thus, generally, we conclude that the conductance variation behavior of mixed CN models will be determined according to the preference ordering of CN11/CN111 > CN1 > CN3/CN2.

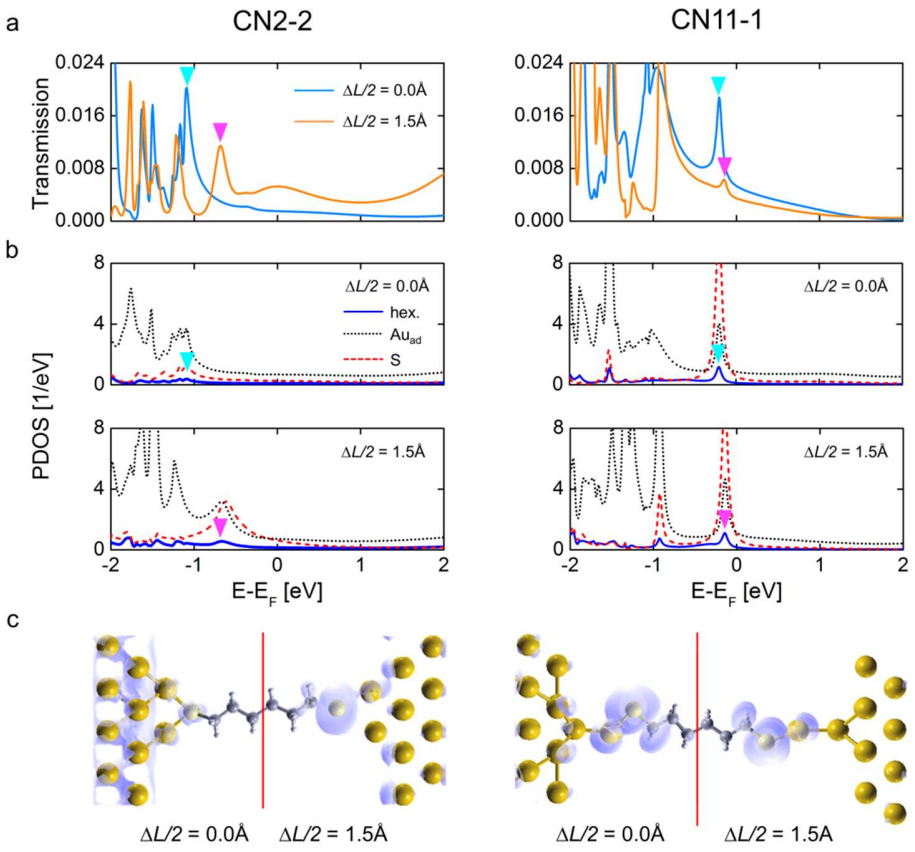

Figure S5 | Electronic structure of the CN2-2 and CN11-1 model. (a) Transmission of the CN2-2 (left) and CN11-1 (right) model at the low and high strain conditions. Cyan and orange solid lines represent the low and high strain conditions, respectively. (b) PDOS plots corresponding to the low (upper) and high (lower) strain conditions. Black dashed lines, blue solid lines, and red dash-dot lines represent hexane core, Au adatoms, and S linker atoms, respectively. (c) LDOS plots around the first S PDOS peaks indicated in (b) with the energy window of (-0.05, +0.05) eV.

D. Analysis of charge redistributions and resulting changes in electrostatic potentials and electric fields across Au-S interfaces

The molecule-electrode bonding-induced charge redistributions were analyzed by the plane-averaged electron density differences,

$$\delta\bar{\rho}(z) = \bar{\rho}_{\mathrm{Au+C6}} \quad (z) - [\bar{\rho}_{\mathrm{Au}}(z) + \bar{\rho}_{\mathrm{C6DT}}(z)],$$

where $\rho_{\mathrm{Au+C6DT}}(z)$, $\rho_{\mathrm{Au}}(z)$, and $\rho_{\mathrm{C6DT}}(z)$ represent the electron densities of Au–C6DT–Au junctions, isolated C6DT molecules, and two Au electrodes along the stretching direction, respectively. The plane-averaged electric potential differences, $\delta\bar{V}$, and field, E, associated with the charge redistributions were calculated by solving the one-dimensional Poisson equation,

$$\nabla^2\delta\bar{V}(z) = -\delta\bar{\rho}(z)/\varepsilon_0 \,,$$

and,

$$\nabla\delta\bar{V}(z) = -E,$$

where ε_0 is the vacuum dielectric constant.

The stretching-induced HOMO peak upshift can be understood in terms of the change of the electrostatic potential generated by bonding-induced charge redistributions at the two molecule – metal contacts. In the case of CN3-3 junction, the electron density accumulating on S atoms was increased with the junction stretching (Supplementary Fig. S6, left panel), which results in the upshift of S-originating HOMO PDOS toward the electrode Fermi level (Fig. 3b, left panels). Similarly, in the CN2-2 junction, the increment of the potential energy within the molecule region was again obtained under the high strain condition. However, the amount was 0.33 eV, which was smaller than 0.61 eV in the CN3-3 case. While the CN1-1 model also showed a slight potential increase upon junction elongation (Fig. S6, left panels), there was no distinct influence of the stretching on both charge redistributions and resulting potential energy profiles in the CN11-11

junction case (Fig. S6, right panels). These findings again correspond well with the negligible HOMO peak upshift (Fig. 3b, right panels), indicating there exists no driving force to increase conductance with junction stretching for the junction models based on Au monoatomic chain contacts.

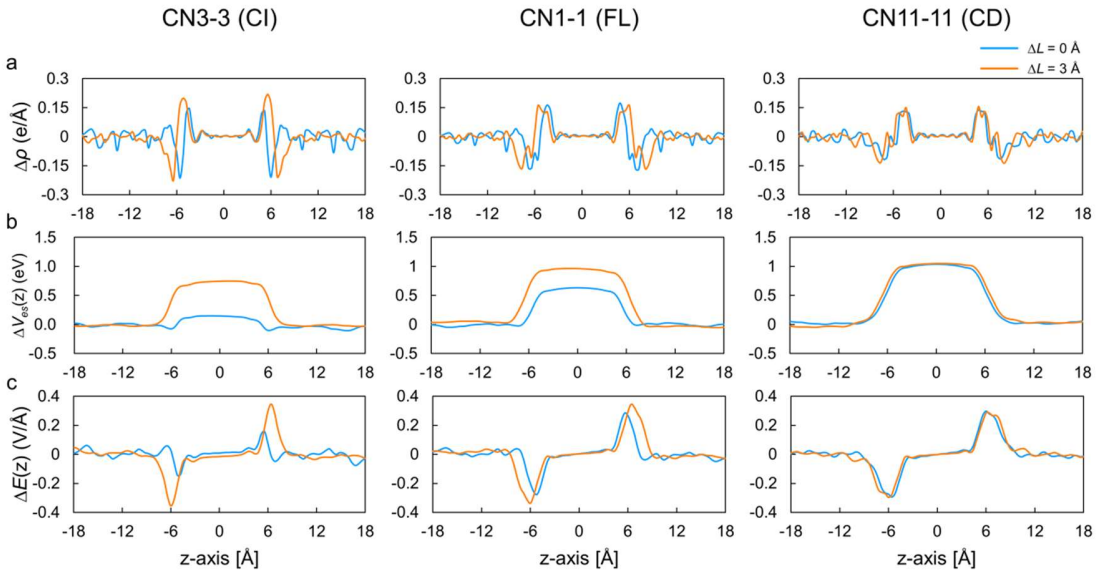

Figure S6 | Bonding-induced charge redistribution at the CN3-3, CN1-1 and CN11-11 junctions. (**a**) The charge redistributions at the Au-S contacts in the CN3-3 (left), CN1-1 (center), and CN11-11 (right) models. See the text for the definition of plane-averaged electron density differences. The corresponding (**b**) electrostatic potentials and (**c**) electric fields obtained by solving the 1D Poisson equation. Cyan and orange solid lines represent the low- and high-strain conditions, respectively.

E. *Ab initio* MD simulation results at different pulling conditions

ΔL [Å]	Time [fs]	Speed [m/s]	CN3 → CN21
0.4	1000	40	○
0.8	2000	40	○
0.2	500	40	○
0.4	500	80	○
0.4	250	160	○
0.4	166	240	○
0.4	143	280	○
0.4	120	333	X
0.4	100	400	X

Table S1 | Effects of displacement magnitude and evolution time (elongation speed) on the occurrence of CN3 to CN21 transformation within DFT-based *ab initio* MD simulation. Here, *Time* is the evolution time during *ab initio* MD simulations and *Speed* corresponds to ΔL / *Time* in the unit of m/s. The CN3 to CN21 transformation was observed for the pulling speed range of 40 ~ 280 m/s. On the other hand, the CN3 contact was ruptured without showing the CN conversion for the pulling speed > 330 m/s.

F. Supplementary Movies

Movie S1 | Contact atomic structure transformation from CN3-3 to CN3-12.

Movie S2 | Contact atomic structure transformation from CN3-12 to CN21-12.

Movie S3 | Contact atomic structure transformation from CN21-12 to CN21-111.

Movie S4 | Contact atomic structure transformation from CN21-111 to junction breaking.

II. Supplementary Experimental Data

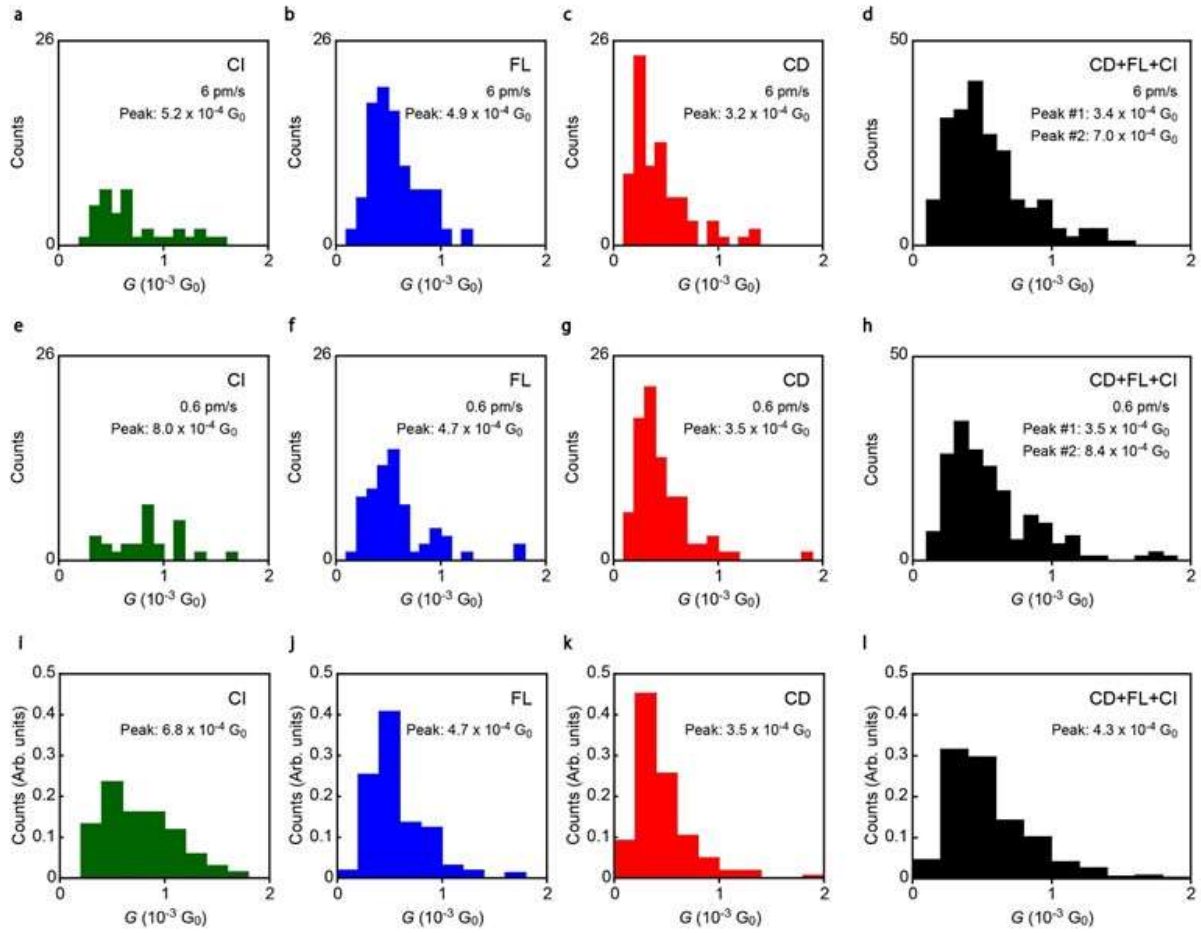

Figure S7 | Conductance histogram separated by pulling speed and type of traces (a-h) Conductance distributions of the three types of traces obtained at the junction stretching rates of (a-d) 6 pm/s and (e-h) 0.6 pm/s. Bin size is 1 x 10^{-4} G_0. **(i-l)** Normalized histograms constructed with the data obtained at 6 pm/s and 0.6 pm/s. Bin size is 2 x 10^{-4} G_0. Average conductance was extracted by Gaussian fit to the plots. Color coding is: green (CI), blue (FL), red (CD), and black (summation of CD, FL, and CI). Data analysis was performed for data above 10^{-4} G_0.